OTKA 105355 final report

Biomaterials used for implant should posses some important properties in order to long-term usage in the body without rejection. One of the most important property is biocompatibility. These materials are used in different parts of the human body as artificial valves in the heart, stensts in blood vessels, replacement implant in shoulders, knees, hips and orodental structures. Materials used as different biomaterials should be made with certain properties as excellent biocompatibility, superior corrosion resistance in body environment, excellent combination of high strength and low modulus, high ductility and be without toxicity. The creation of nanocomposites of ceramic materials with particle size few ten nanometers can significantly improve the bioactivity of the implant and enhance the osteoblast adhesion.

One of the most used biomaterial is hydroxyapatite. The major inorganic constituent of bones and teeth is calcium phosphate, whose composition is similar to that of synthetic hydroxyapatite (HAp; $Ca_{10}(PO_4)_6(OH)_2$. This similarity provides HAp based materials excellent bioactivity like bone bonding capability, osteoconductivity, and biocompatibility.

Hydroxyapatite is a very attractive material for human hard tissue implantation, because is the main constituent (up to ~69%) of the human bone. Unfortunately HAp alone posses low mechanical properties (strength, fracture toughness), which is a barrier to its applications in load-bearing applications. Combination of HAp with other materials to form composites with higher strength and toughness is one solution in order to improve the intrinsic properties of HAp. In the other hand it is becoming widespread to place a HAp coating layer on metallic implants. In case of HA composites, the mechanical properties are related to the synthesis conditions, parameters of preparations, the second phase properties and matrix-addition interactions. The second phase used in our experiments yttria stabilized zirconia (ZrO_2) exhibits high toughness and has wide applications in bone surgery, because it is classified as a bioinert ceramic e.g. for knee joints. Moreover, HAp–ZrO_2 composites showed improved fatigue resistance in addition to high strength.

On the other hand the poor mechanical properties of sintered HAp can be overcomed by the development of a composite with nanosized grain structure. Nanosized HAp particles can also accelerate the sintering kinetics due to higher surface area and hence improved mechanical properties. Other possible ways to overcome the mechanical limitations include the incorporation of some reinforcement phase in the HAp matrix along with a reduced sintering temperature to avoid chemical decomposition. Among reinforcing fillers glass, alumina or various carbon nanosturctures, such as carbon nanotubes or graphene nanoplatelets have been investigated.

A successful electrodeposition method for preparing silver and zinc modified bioactive calcium phosphate layers onto surgical grade titanium alloy material (Ti6Al4V) was also developed. The coatings were deposited on the Ti6Al4V surface by pulse current at 70°C from an electrolyte containing adequate amounts of calcium nitrate, ammonium dihydrogen phosphate, zinc nitrate and silver nitrate. The corrosion resistivity of the bioceramic coatings was assessed in conventional Ringer's solution in a three electrode open cell by potentiodynamic polarization and electrochemical impedance spectroscopy (EIS) techniques. The results revealed the pure bioactive calcium phosphate (CaP) coated implant materials to possess the highest resistivity to corrosion, while the silver and zinc doped CaP layer showed at least one order of magnitude lower corrosion resistance. These modified CaP coatings can be further considered as antimicrobial coatings with enhanced biocompatibility.

The morphology and structure of the coatings were characterized by Scanning electronmicroscopy (SEM), Energy-dispersive X-ray spectroscopy (EDX) and X-ray diffraction (XRD) that confirmed the pulse current deposited CaP layer to consist of a mixture of different calcium phosphate phases such as hydroxyapatite (HAp), monetite (dicalciumphosphate, $CaHPO_4$) as well as other Ca-containing components, portlandite (Ca $(OH)_2$) and parascholzite ($CaZn_2(PO_4)_2(H_2O)_2$).

Titanium (Ti) is most commonly used as orthopedic implant materials or bone substitute materials. Ti has good biocompatibility and sufficient mechanical properties for medical applications. One negative property of Ti is a low abrasion resistance and minute Ti abrasion powders may cause inflammatory reactions. Biomaterials must be chemically inert, stable and mechanically strong enough to wishstand the repeated forces of a lifetime. From this point of view, TiC is a very stable phase in comparision to pure Ti or Ti alloys. Titanium carbide (TiC) is useful material for biomedical instruments because has a range of desirable properties. In this project, the combination of excellent bioactive hydroxyapatite with very stable and mechanicaly strong TiC has been studied. The nanostructured hydroxyapatite has been prepared by high efficient milling starting from biogenic eggshells. TiC thin films were deposited by dc magnetron sputtering in argon atmosphere at different deposition temperatures. Spin coating was applied to obtain HAp decorated TiC films. Structural, mechanical and biological properties of HAp, TiC and TiC/HAp coatings have been investigated in this study.

The major aims of this research project was:

1) Preparation of hydroxyapatite and other calcium phosphate powders and thin films from natural raw materials (eggshell or seashell) by using the powder technology. Understanding of hydroxyapatite based powders and films evolution mechanism.
2) Porous and compact hydroxyapatite based materials will be realized by different sintering techniques (HIP, SPS). Structure, mechanical – biological properties relation will be examined.
3) Biological evaluation of the hydroxyapatites (eggshell and seashell) and synthetic raw materials. Control of structure (porosity, crystallinity, morphology, composition, structural routhness at sintered composites) will be also studied and optimized.
4) To explore the synergetic combination; zirconia and graphene have been applied as reinforcing agents to hydroxyapatite matrices. Our investigations will focus on reinforcing mechanisms and to optimization of composite processing-structure-properties relationship.
5) We focused to preparation among others to ceramics with high interest in human implant fields namely TiC coatings and silicon nitrides (reinforced with graphene).

Preparation of hydroxyapatites

Eggshells ans seashells were collected and washed with detergent, then calcined in air at 900°C for 10 h. During the first 30 minutes most of the organic materials were burnt out, then the eggshells were converted to calcium oxide. Calcined shells were crushed and milled in a ball mill or an attritor mill. The ball mill was equipped with alumina balls and bowls, the attritor mill was fitted with zirconia tanks and zirconia balls (Ø2 mm). The crushed eggshells were reacted with phosphoric acid (H_3PO_4) in an exothermic reaction. The mixtures were milled for 5 h at 4000 rpm (attritor milling) or for 10 h at 350 rpm (ball milling), to achieve homogenous mixtues and to prevent agglomeration. In all cases, the used shell: H_3PO_4 ratio was 50:50 wt%. After milling, a small amount (approximately 0.5 g) of each type of HAp powder was sintered at 900°C for 2 h in air. HAp powders usually degrade at high temperatures, the most common problem being CaO formation.

Structural investigation of hydroxyapatite

The structural investigations were studied by scanning electron microscope (SEM, LEO 1540 XB) and transmission electron microscope (TEM, Philips CM-20). The eggshell structure was relatively compact with average grain size about 3 μm. The XRD measurement of the calcined eggshell confirmed mainly the CaO (JCPDS-PDF 0371497) phase. The effect of various milling was observed after attritor and ball milling. SEM image of powder prepared by attritor is shown in Fig. 1a. The SEM investigation confirmed that the attritor milling is more efficient in grain size reduction than ball milling. Thus, smaller particle size with homogeneous size distribution may be achieved with attritor milling. In both cases, the grains were agglomerated. The XRD measurements of powders prepared by two different milling showed different phases (Fig. 1b). In the both cases, the powders are consisted of hydroxyapatite (HAp, JCPDSPDF 74-0565), calcite ($CaCO_3$, JCPDS-PDF 05-0586), calcium hydroxide ($Ca(OH)_2$, JCPDS-PDF 01-0653).

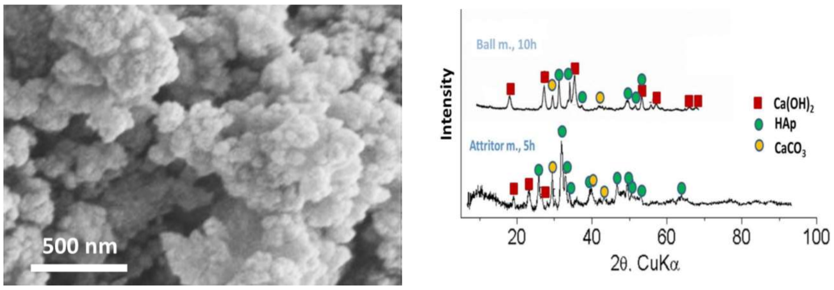

***Fig. 1.** SEM images of milled eggshells. a) attritor mill at 5h, 4000 rpm, XRD results of milled powders b).*

The reduction of average particle size of milled powders from few hundred nm to 100 nm was observed after heat tretment at 900°C during 2h. The agglomeration is still present, but the size of agglomerates is lowered (Fig. 2). Smooth surfaces are evolving after heat treatment at 900°C in the case of ball milling.

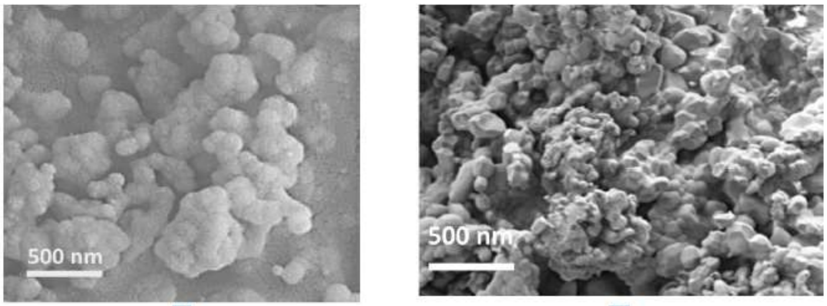

a) b)

***Fig. 2.** SEM images of milled powder after 2h heat treatment at 900°C. a) attritor b) ball mill*

Fig. 3. shows X-ray diffractograms of the milled powders after heat treatment at 900°C during 2h. Only two phases were observed; the main phase hydroxyapatite (HAp) and minor phase calcium oxide (CaO, JCPDS-PDF 037-1497).

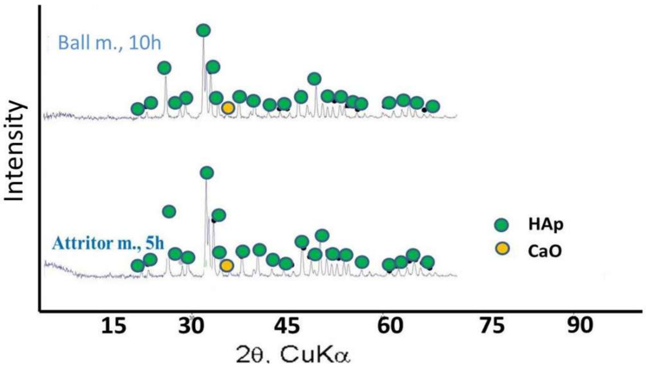

***Fig. 3.** XRD measurements of milled and treated powders. a) attritor, b) ball mill.*

The phase composition of powders was studied by Fourier transform infrared spectroscopy (FTIR-Varian Scimitar FTIR spectrometer equipped with broad band MCT detector). The FTIR spectrum after attritor milling (Fig. 4) resembles the characteristic spectral feature of bone mineral. The spectrum is dominated by the typical PO_4 bands of poorly crystalline apatite phase components of the triply degenerated υ_3PO_4 asymmetric mode at 1021 and 1087 cm^{-1}(shoulder), nondegenerated symmetric stretching mode of υ_1PO_4 at 962 cm^{-1} and components of the triplet of υ_4PO_4 bending mode at 599 and 562 cm^{-1}. Carbonate bands are also observed at 1550–1350 cm^{-1} (υ_3), 873 cm^{-1} (υ_2) and 712 cm^{-1} (υ_4). By analogy with bone mineral, the position of carbonate bands (1456, 1415 and 872 cm^{-1}) indicates the formation of a carbonated apatite with B-type substitution (in tetrahedral positions). The broad band of low intensity in the range 3000–3400 cm^{-1} can be attributed to traces of water incorporated to the structure, together wit the very weak, broad band around 1640 cm^{-1} of H–O–H bending mode. In the OH stretching vibration region, beside the υOH of HAp, surface OH band at 3644 cm^{-1} also appears, probably connected to CaO occurring on the surface. In the case of attritor milled and treated powder, the intensity of surface OH band also increases with increasing the temperature (Fig 4).

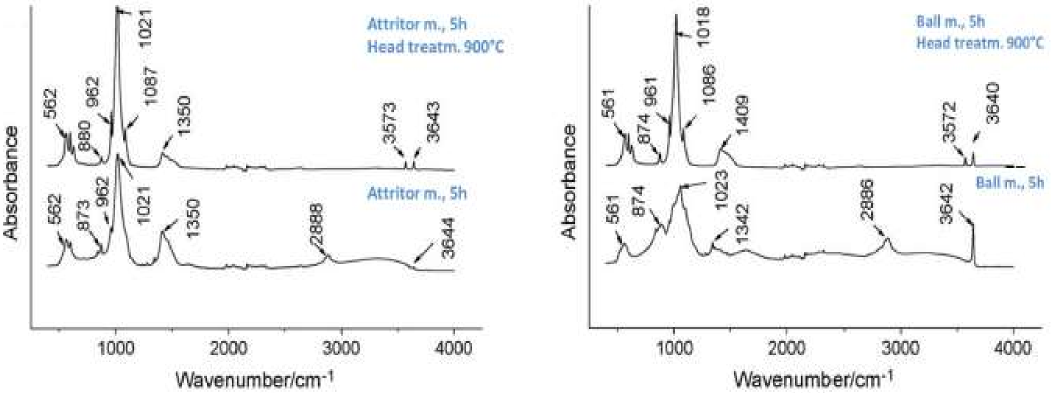

a) b)

Fig. 4. *FITR spectra of milled and heated powders, a) attritor, b) ball mill.*

FTIR spectrum of ball milled powders shows a complex mixture of different calcium phosphate phases (Fig. 4). This band decreases in matured bone apatite and in highly crystalline HAp. The pure HAp phase with some carbonate substitution is formed only after 900°C. However, surface OH bands are also present in the spectrum. After heat treatment, spectral features of the apatite phase become dominant and above 800 – 900 °C beside some peaks of carbonate (υ_3 at 1466 and 1409 cm^{-1}, υ_2 at 874 cm^{-1}, υ_4 at 713 cm^{-1}) and surface –OH (nOH at 3640 cm^{-1}) typical bands of well-crystallised HAp can be observed (υ_3PO_4 at 1086 and 1018 cm^{-1}, υ_1PO_4 at 961 cm^{-1} and the triplet of υ_4PO_4 at 626, 599 and 561 cm^{-1}). No traces for acid phosphate (HPO_4^{2-} peak around 540 – 530 cm^{-1}), characteristic for immature bone mineral or incomplete apatite phase can be observed.

Biological properties of hydroxyapatite

Thirty 12-week-old Sprague-Dawley rats were used for this animal study. This experiment was approved by the Institutional Animal Care and Use Committee of Gangneung-Wonju National University, Gangneung, Korea (GWNU-2012-11). General anesthesia was administered by the intramuscular injection of a combination of Zoletil 50® (15 mg/kg; Vibac Korea, Seoul, Korea) and Rompun® (0.2 mL/kg;Bayer Korea, Seoul, Korea). The cranium area was shaved and disinfected with povidine-iodine. A longitudinal midline incision was made in skull. Sharp subperiosteal dissection was performed to expose the parietal bone. A dental trephine bur was used under copious saline irrigation to create a fullthickness calvarial defect. After the formation of a round parietal bony defect (diameter: 8.0 mm), either seashell derived sHAp or eggshell derived eHAp was grafted into the bony defect (Fig. 5). The defect in the control was left unfilled. Amount of grafted sHAp or eHAp was the same (0.2 mg) on the each defect, and then, it was uniformed on the entire defect with the use of the small amount of saline. Each group was composed of 10 animals (10 defects for each group). After grafting, the pericranium and skin were sutured with 3-0 black silk. Five animals in each group were sacrificed at 4 weeks and at 8 weeks after the operation. The calvarial specimens were fixated in 10% formalin. These were decalcified by 5% nitric acid for 3 days. The parietal bones were separated through the midline sagittal suture. Both segments were embedded to show the sagittal sections in the paraffin blocks. Then, the sections were sliced and stained with Masson-trichrome.

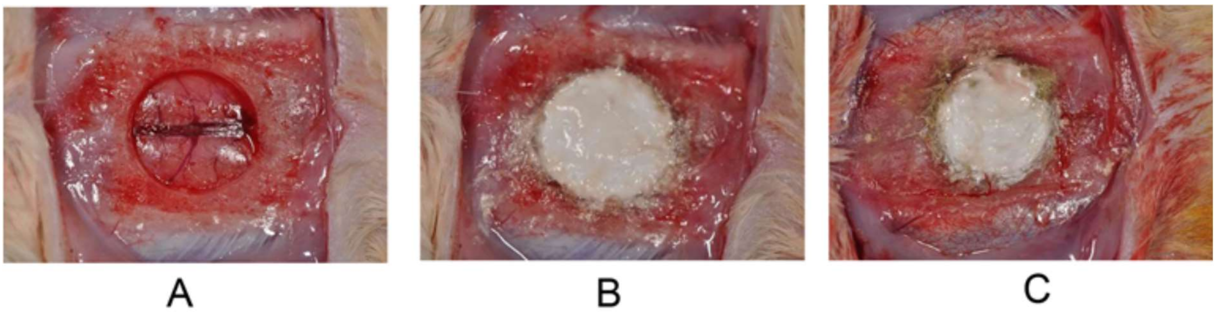

Fig. 5. *Images of animal experiment. (A) Preparation of 8 mm-diameter round parietal bone defect. (B) The sHAp was grafted into the bone defect. (C) The eHAp was grafted into the bone defect.*

The prepared specimens underwent μ-CT using a Skyscan 1076 (Aartselaar, Belgium). The calvarial specimens were scanned in 0.035 mm thick sections after calibration. The scanned images were reconstructed by CT-AN 1.10 software (Skyscan). The calibrated 3-dimensional images were shown in the gross proles of the specimens. The setting of the region of interest (ROI) was considered to be the initial defect size and shape, because the initial defect was round in shape with an 8.0 mm diameter. A threshold level of 25% of the bone standard was set, as recommended by the manufacturer. The ROI of each specimen was analyzed for bone volume (BV) and bone mineral density (BMD). The analysis of variance (ANOVA) test was applied for the comparison of these groups and the least significant difference (LSD) was used as a post hoc test. The signicance level was set at $p < 0.05$.

ICP-OES was used for the elemental analysis of the powder. The sodium (Na) and strontium (Sr) contents were significantly higher in the case of sHAp. The concentration of Na was 3177.92 mg/kg and 1512.52 mg/kg in the sHAp and eHAp, respectively. The Sr content was 2187.57 mg/kg and 411.88 mg/kg in the sHAp and eHAp, respectively. The differences between the other elements were not remarkable. In contrast, a higher magnesium (Mg) content was measured in eHAp. The measured Mg content was 165.79 mg/kg and 3472.84 mg/kg in the sHAp and eHAp, respectively.

The results of μ-CT are shown in Fig. 6. The mean bone mineral density (BMD) value was 0.72 ± 0.02 g/cm^3, 0.67 ± 0.06 g/cm^3, and 0.57 ± 0.13 g/cm^3 in the sHAp, eHAp, and control group at the 4 weeks after the operation, respectively. Significant differences among the groups ($p = 0.036$) were observed. According to post hoc tests, the difference between sHAp and the control group was significantly different ($p = 0.012$). The mean BMD was 0.69 ± 0.08 g/cm^3, 0.75 ± 0.07 g/cm^3, and 0.69 ± 0.08 g/cm^3 in the sHAp, eHAp, and control group, respectively, at 8 weeks after the operation. No significant difference among the groups ($p > 0.05$, Fig. 7) was observed.

The mean bone volume (BV) was 3.51 ± 1.89 mm^3, 4.34 ± 2.43 mm^3, and 2.52 ± 1.13 mm^3 in the sHAp, eHAp, and control group, respectively, at 4 weeks after the operation.

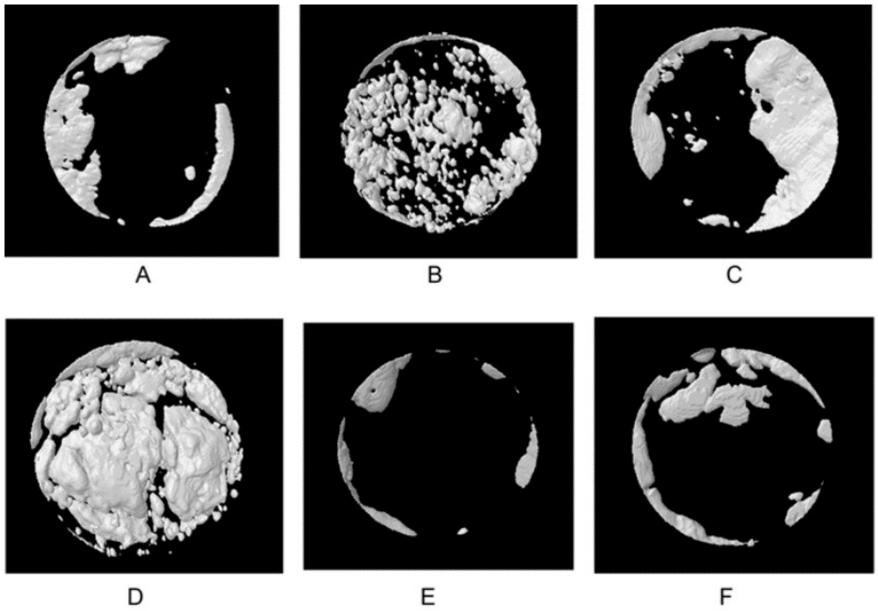

Fig. 6. *Images of micro-computerized tomography. (A) The sHAp graft at 4 weeks after the operation. (B) The sHAp graft at 8 weeks after the operation. (C) The eHAp graft at 4 weeks after the operation. (D) The eHAp graft at 8 weeks after the operation. (E) The unfilled control at 4 weeks after the operation. (F) The unfilled control at 8 weeks after the operation.*

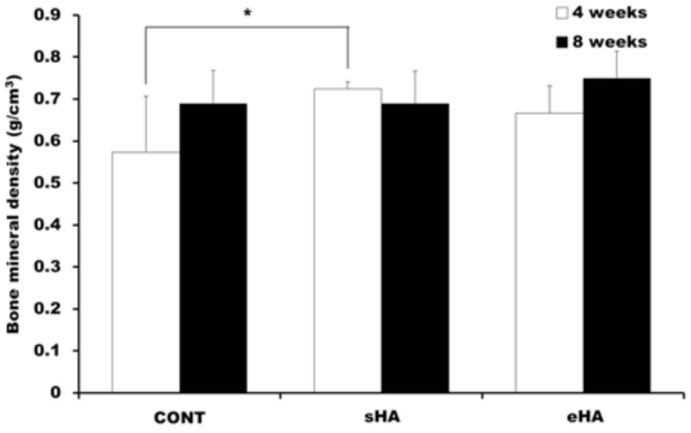

Fig 7. *The results of bone mineral density from micro-computerized tomography analysis. (**, $p < 0.05$)

There were no significant differences among the groups ($p > 0.05$). The higher mean BV with significant differences among the groups ($p = 0.039$) was measured at 8 weeks after the operation: 10.20 ± 7.24 mm^3 for sHAp, 15.59 ± 7.23 mm^3 for eHAp and 4.20 ± 2.85 mm^3 for the control. According to post hoc tests, the difference between the eHAp and control groups was significantly different ($p = 0.012$, Fig. 8).

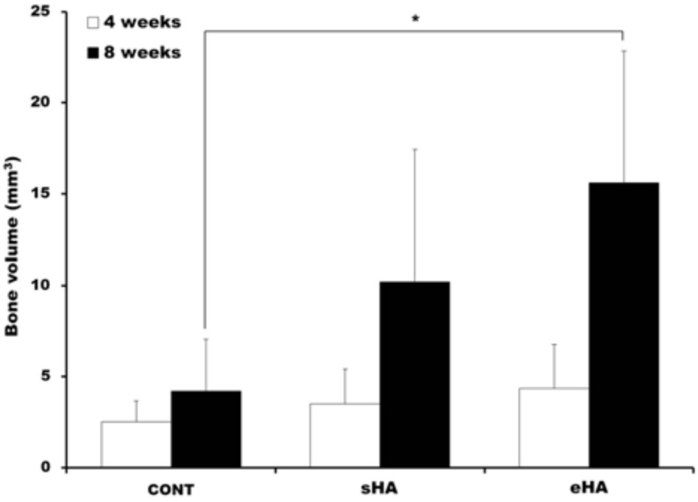

Fig. 8. *The results of bone volume from micro-computerized tomography analysis. (*, $p < 0.05$)*

In the histological images, the unfilled control showed less bone regeneration compared with the sHAp-and eHAp-grafted groups at 4 and 8 weeks after the operation (Fig. 9). The regenerated new bones were observed around the remaining agglomerated particles of the sHAp and eHAp at 8 weeks after the operation (Fig. 9 G, H, K, L). New regenerated bones encircled agglomerated eHAp particles and grew into the interspace of eHAp agglomerates at 8 weeks after the operation (Fig. 9 K, L). However, in the case of sHAp, many foreign body multinucleated giant cells were observed around the agglomerated particles at 4 and 8 weeks after the operation (Fig. 9 E-H).

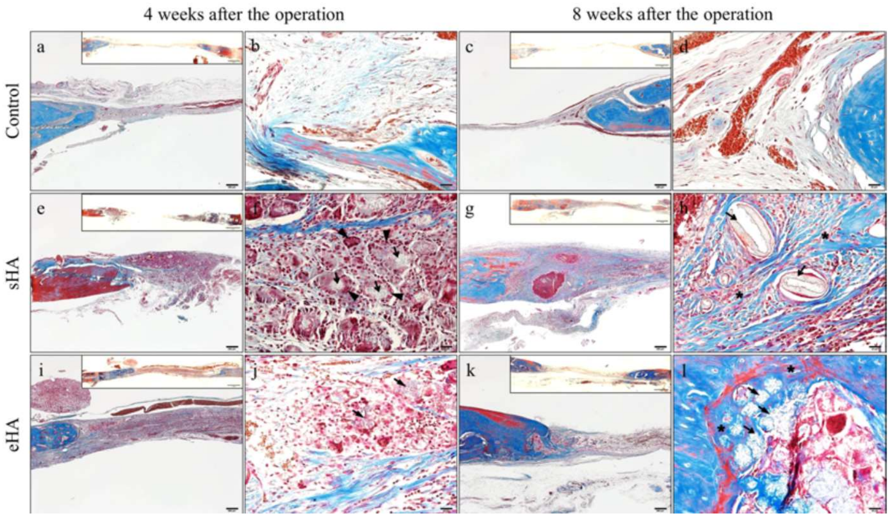

Fig. 9. *Histological images of sHAp, eHAp, and control groups. (A, B) The sHAp graft at 4 weeks after the operation. (C, D) The sHAp graft at 8 weeks after the operation. (E, F) The eHAp graft at 4 weeks after the operation. (G, H) The eHAp graft at 8 weeks after the operation. (I, J) The unfilled control at 4 weeks after the operation. (K, L) The unfilled control at 8 weeks after the operation. (A, C, E, G, I, and K, low magnification view, bar = 200 μm; B, D, F, H, J, and L, high magnification view, bar = 20 μm.) The images located on the right upper corner of low magnification images showed whole defect area of each samples (bar = 1 mm). (open arrow, particles of the sHAp or eHAp; closed arrow, multinucleated giant cell; asterisk, new regenerated bone surrounding sHAp or eHAp)*

Preparation method of biopolymer-hydroxiapatite composite

Nanosized HAp powder was synthesized from raw materials. The as-received HAp powder was added to acetic acid forming a 9.38% wt/vol solution. This solution was then mixed with CA solution, which was CA powder dissolved in acetone to form 15% wt/vol.composition.

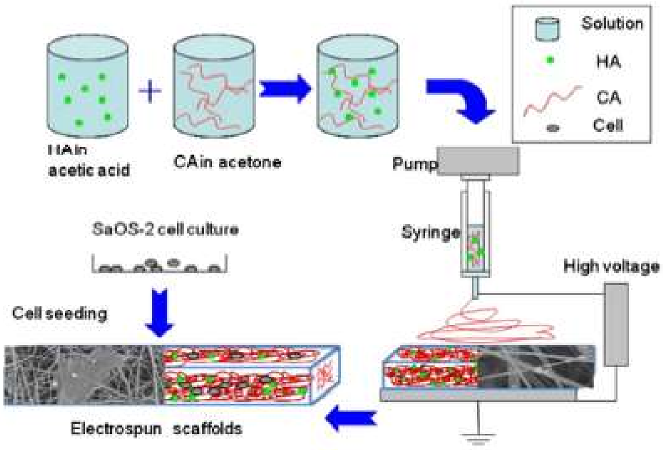

Fig. 10 *Schematic view of polymer – Hap biocomposite preparation*

The mixed solution (71–29 vol.% acetone /acetic acid) was introduced into a standard vertical electrospinning setup and was electrospun by KDScientific KDS202-CE electrospinnig device with high voltage supply. The needles were common medical needles, which ending-points were polished perpendicular to the direction of the flow. The polymer was cellulose-acetate (CA) (22188; M_r~29000 {9004-35-7}; Fluka/Sigma-Aldrich), the applied solvents were acetone (Spektrum3D), isopropanol (Reanal), and acetic-acid (Spektrum3D), flow rate 9.6 mL/h, voltage 19 kV and distance from needle to collector 10 cm.

Structural properties of polymer - HAp composite

Stuctural investigations showed that the diameter of the fibers is nearly uniform, about 200-800 nm, but too many beads were formed and spheres developed with a few hundred microns in diameter (Fig. 11). The EDS confirmed that the fibers contain the HAp, but the element mapping shows that the distribution of it is not homogenous. The EDS measurement showed C (found in CA), O (CA and HAp), P (HAp), Mg, S (HAp-eggshell trace element) Si (sample holder) and Al (sample cover) compounds. According to the Ca and P element maps the HAP presence in 1-2 micrometer sized clusters. The presence of Ca and P can be in 1-2 micron clusters. The distribution of O in the CA fibers is homogeneous.

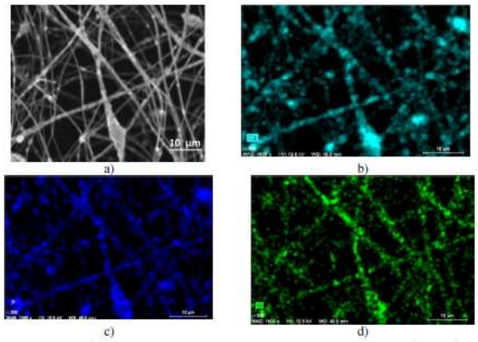

Fig. 11. *Structural investigation of CA- HAp composite. a) SEM images, b) Elemental map of Ca, c) Elemental map of P, d) Elemental map of O.*

From our study, deal parameters were between 15 and 25 w/w% solid material (HAp+CA), increasing the concentration affects larger fiber diameter and fewer beads. Using more than 30 w/w% and less than 5 w/w% it was impossible to produce fibers. Applying 20 w/w% acetic-acid electrospinning process generated uniform fiber diameter. Using any other w/w% acetic-acid caused larger fibers diameter and more beads. It could be concluded that the composition of the solution has the most striking influence on the morphology of the final mats.

Our studies suggest that the morphology and structure of the CA-HAp composite scaffolds play important roles in facilitating cell spreading and differentiation and enhance apatite mineralization. Based on our observations, the electrospun CA scaffolds with nanosized HAp are considered as a promising candidate for bone tissue engineering application.

Preparation of HAp-zirconia composites

Hydroxyapatite and 8 mol% yttria stabilized zirconia were the two base materials used in this study. HAp powder was made by reacting heat treated eggshell and ortophosphoric acid, the details of the process has been published in earlier works. The HAp powder has 100–200 nm grain size, but according to the high specific surface activity the grains agglomerate and form 5 to 20 micron size particles (Fig. 12).

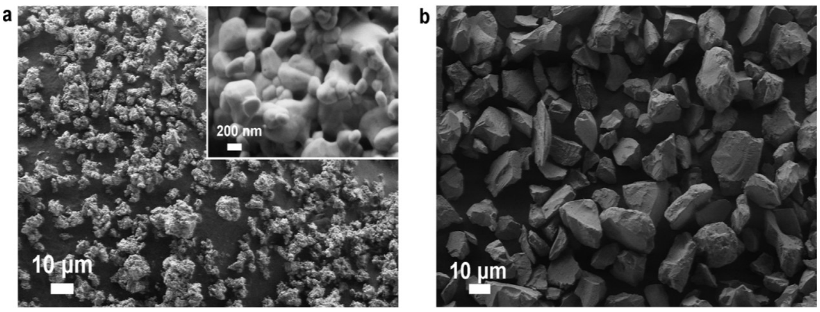

***Fig. 12**. Scanning electron micrographs of base materials: (a) HAp, (b) ZrO2.*

We did perform the oxidation resistence observation on the eggshell derived HAp in earlier studies. The result showed that HA is preserving the original crystalline structure even after oxidation 900 ◦C for 2 h in air atmosphere. Also it was shown that over 900 ◦C the eggshell derived HAp have a tendency to phase transformation (TCP). According to the X-ray measurements some CaO was formed in HAp. The as prepared HAp was demonstrated to be a competitive high bioactive bone graft in in vivo experiments. On the other hand a commercial yttria stabilized zirconia (ZrO_2–8 mol%Y_2O_3) powder (Amdry 6643) was used in the as provided state with 45 ± 11 micron size particles (Fig. 12). The HAp and ZrO_2 powders were mixed by attritor milling for 2 h (at 4000 rpm) to obtain a homogeneous powder mixture. The powders were subsequently densified by the spark plasma sintering process on a Dr. Sinter SPS 7.40 MKVII system (Sumitomo Coal Mining Co., Japan). Powders were loaded on a graphite die (50 mm in diameter) and punch unit and heated to a predetermined temperature at a heating rate of 100 ◦C/min. The applied mechanical pressure was 30 MPa, experiments have been performed in vacuum. After dwelling for 5 min the pressure was released and the samples were cooled to room temperature. The microstructure of the spark plasma sintered composites was investigated by LEO 1540 XB scanning electron microscope (SEM). The crystal phase of the powder was determined by Xray diffraction (XRD), using CuKalfa radiation (Bruker Advance 8D).

As a result high hydroxyapatite content (60, 90, 95 and 100 wt% HA) HA–ZrO_2 composites were prepared by spark plasma sintering at two different (600 and 950 ◦C) sintering temperature. The reason of using relative low temperature was to avoid the decomposition of hydroxyapatite. The results are summarized as follows:

(a) According to the XRD results, HA phase can be maintained and other main compound than hydroxyapatite–zirconia (not counting the minor $CaCO_3$ phase) was not formed after the spark plasma sintering.

(b) A layered microstructure was formed in the samples very probable due to the inhomogeneous pressure in SPS also demonstarted in earlier literature work. The marginal parts of the samples showed good sintered surface with small macro-and micropores, while the middle part of the samples contained larger porosities and large hexagonal grains.

(c) The marginal parts of the samples had an excess carbon content, which was diffused from the graphite die, so this phenomenon was also derived from sintering method.

(d) The samples with 10–40 wt% ZrO_2 are showing only closed porosity.

(e) The hardness of the composites could be strongly related to the density of composites. The highest bending strentgh (125 MPa) was obtained in the case of the highest ZrO_2 content (40 wt%) sintered at 825 ◦C.

Electrochemical deposition of calcium phosphate layers

In our study electrodeposited silver and zinc doped calcium phosphate layers on metallic implant material have been examined.The electrodeposition processes have been performed with t-on (deposition time) and t-off (relaxation time) in the millisecond range.The corrosion properties and biodegradation ability characteristics of layers have been measured by complex electrochemical methods,while the morphology and structure of the layers have been studied by SEM, EDX and XRD measurements.

XRD patterns of pure and modified CaP coatings are shown in Fig. 13. The straight base line and sharp peaks on the diffractograms confirmed the layers to be partially crystallized. Pattern a was recorded on pure calcium phosphate layer, pattern b on silver doped CaP layer, pattern c on zinc doped CaP layer while pattern d on silver and zinc doped CaP layer. The main peaks can be identified as a mixture of calcium phosphate phases such as hydroxyapatite (HAp, JCPDS76-0694) and monetite or dicalcium phosphate (DCP, JCPDS89-5969) as well as calcium hydroxide (portlandite, JCPDS44-1481).The main reflections of HAp component are at d=2.814 Å and d=2.719 Å. The DCP component's main peaks appear at d=3.349 Å and d=2.726 Å, while in portlandite the main peaks are at d=2.627 Å and d=1.926 Å. In case of silver doped CaP phases, the most intensive peak of Ag (111) appears on the spectra (Ag:JCPDS89-3722) at d=2.358Å. In this case the silver particles are present in the layer in metallic form.

The XRD patterns of Zn and Ag/Zn modified CaP layer (Fig. 13c,d) showed the Zn particles to be found in two main structures in the layers, one of them is metallic Zn (Zn:JCPDS87-0713) while the other Zn containing component can be identified as $CaZn_2(PO4)_2(H_2O)_2$ (Parascholzite, JCPDS86-2372).The reflections of main peaks of metallic zinc component and parascholzite are at d=2.091 Å and at d=4.156 Å,respectively.

It is visible on Fig. 13d that in silver and zinc containing CaP layer there is no detectable metallic zinc present, which can be explained by the favored formation of calcium zinc phosphate hydrate component at lower Zn^{2+} concentrations in the electrolyte during deposition.

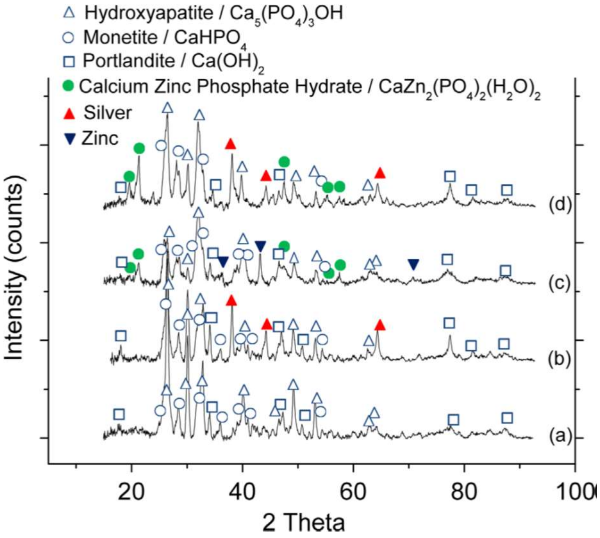

Fig. 13. *XRD patterns of pure CaP layer (a) Ag_CaP layer (b) Zn_CaP layer (c) and AgZn_CaP layer (d).*

Structural investigation of TiC/a:C thin films

TiC based nanocomposites have been deposited between 25 °C and 800 °C. As it has been showed, the nanocomposite film deposited at 200 °C exhibited the best mechanical properties (nanohardness 18 GPa and elastic modulus 205 GPa). The film consisted of TiC crystallites separated by thin carbon matrix (Fig. 14) as showed by TEM investigations. The crystallites have columnar structure with average width around 10–15 nm. The mechanical properties of films, namely hardness and elastic modulus may be compare with mechanical properties of bulk Ti implants. In the case of TiC film, the 18 GPa hardness and 205 GPa elastic modulus value was measured. TiC phase was the reinforcing phase to enhance the hardness of films. Highest H/E ratio ~ 0.094 and elastic recovery ~ 0.634 indicate that the deformation of the TiC nanocomposites arises mainly from elastic deformation of the C matrix which determines the elasticity of the asperities in a tribological contact.

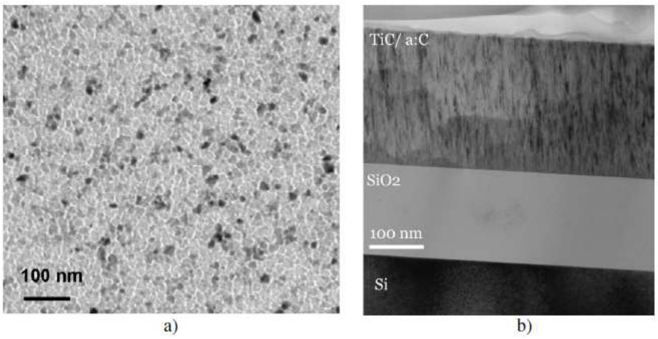

a)

b)

Fig. 14. *TEM investigation of TiC/a:C thin film prepared at 200°C. a) plan view TEM image, b) cross-section TEM image.*

Selected area electron diffraction (SAED) confirmed the stable cubic TiC phase, JCPSFWIN 32-1383). The optimal content from the structure (crystallites separated by thin carbon matrix) of the doped C films is one with a low metal concentration within 1–20 at.%. EDS elemental analysis of the film composition resulted in ~62–72 at.% C and 23–26 at.% Ti composition of the films.

Biological properties of TiC based thin films

The *in-vitro* tests of biocompatibility and bioactivity of TiC coatings were studied on the adhesion, growth, maturation, viability, stress adaptation and potential immune activation of osteogenic cells in cultures on these materials. For the cell culture experiments, the samples have been sterilized with 70% ethanol, inserted into 24-well polystyrene cell culture plates (TPP, Switzerland; internal well diameter 15.6 mm). These studies were carried out on human osteoblast-like cell line MG-63 (European Collection of Cell Cultures, Salisbury, UK). The cells have been cultured for 1, 3, and 7 days at 37 °C in a humidified air atmosphere containing 5% CO_2. For the cell culture experiments, glass slides and also the bottom of standard polystyrene cell culture dishes have been used as reference materials.

TiC/a:C nanocomposite thin films did not lead to an increase in cell number after 1 day (Fig. 15a) in culture in comparison with the control microscopic glass coverslips. However, on days 3 and 7 after seeding, the cell numbers on TiC/a:C surface have been found to be similar to PS and significantly higher than that on the microscopic glass coverslips (Fig. 15). The investigated the biological properties of Ti–6Al–4V alloy after surface treatment by the electric discharge machining (EDM) process using MG63 osteoblast cells.

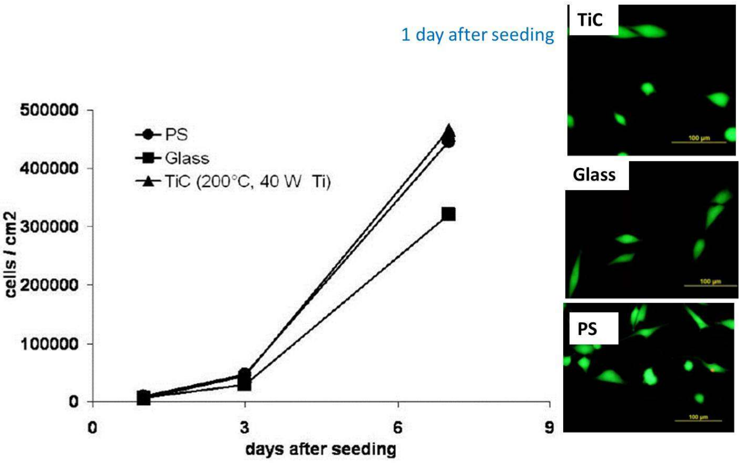

***Fig. 15** The growth dynamics of number of MG 63 cells on day 1, 3 and 7 after seeding. PS - polystyrene dishes, Glass – glass dishes.*

The sputtered TiC/a:C nanocomposite thin films were prepared as potential barrier coating for interfering of Ti ions from pure Ti or Ti alloy implants. Columnar TiC crystallites with 15–20 nm width have been embedded in 5 nm thin amorphous carbon matrix. MG63 osteoblast cells have been used for in vitro study of nanocomposites. The 7 day lasting tests showed a higher value of cells on TiC/a:C nanocomposite surface. On the other hand, the cells on TiC/a:C film showed amore spreading tendency than the cells on control. The distribution of osteocalcin on microscopic glass coverslip did not reach the intensity of osteocalin in cells on TiC/a:C films. concerning all tested materials.

The results of OTKA 105355 have been utilized in EU FP7 Hyporth project.